

Beyond Uncertainty: Risk-Aware Active View Acquisition for Safe Robot Navigation and 3D Scene Understanding with FisherRF

Guangyi Liu*, Wen Jiang*, Boshu Lei*, Vivek Pandey, Kostas Daniilidis, and Nader Motee

Abstract—This work proposes a novel approach to bolster both the robot’s risk assessment and safety measures while deepening its understanding of 3D scenes, which is achieved by leveraging Radiance Field (RF) models and 3D Gaussian Splatting. To further enhance these capabilities, we incorporate additional sampled views from the environment with the RF model. One of our key contributions is the introduction of Risk-aware Environment Masking (RaEM), which prioritizes crucial information by selecting the next-best-view that maximizes the expected information gain. This targeted approach aims to minimize uncertainties surrounding the robot’s path and enhance the safety of its navigation. Our method offers a dual benefit: improved robot safety and increased efficiency in risk-aware 3D scene reconstruction and understanding. Extensive experiments in real-world scenarios demonstrate the effectiveness of our proposed approach, highlighting its potential to establish a robust and safety-focused framework for active robot exploration and 3D scene understanding.

I. INTRODUCTION

The growing need for robots to function effectively in unpredictable and dynamically changing environments, such as disaster zones, and search and rescue operations, necessitates significant advancements in active perception. In these dynamic environments, robots face a dual challenge: exploring their surroundings to build an accurate 3D scene model, e.g., Radiance Field (RF) models [16, 9], while prioritizing their safety and ensuring mission success [4]. To obtain a higher-quality model, robots actively gather additional samples from the environment, a process known as the next-best-view selection problem in the context of Radiance Fields models. Existing methods for selecting the next-best-view for building enhancing RF models [18, 19, 29, 27] prioritize the overall efficiency of scene reconstruction. However, these approaches often neglect crucial safety considerations, potentially exposing the robot to environmental hazards or compromising its operational integrity.

This work leverages Radiance Field (RF) models with 3D Gaussian Splatting [9] for initial 3D scene construction. We then incorporate the perceived environmental map while simultaneously evaluating its inherent uncertainty, similar to the approach presented in [7]. By applying notions of risk measures [21, 14] to this uncertain environment, we can effectively quantify the risk associated with different

areas. Our approach leverages a technique called Risk-aware Environment Masking (RaEM) to prioritize and focus on potential viewpoints in high-risk areas of the environment. This is achieved by effectively masking out areas deemed safe. We then utilize an approach similar to FisherRF [7] to select the next-best-view from a set of candidate viewpoints. This selection process maximizes the expected information gain, focusing on areas with the most significant potential for reducing uncertainty. Through these combined steps, we aim to refine the existing methods for the next-best-view selection. Our method dynamically adjusts the focus of the perception model based on the anticipated risk the robot faces in an uncertain environment.

In our proposed methodology, we convert the perceived 3D environment, represented by 3D Gaussian point clouds, into random variables, capturing the distance between the robot and different parts. This allows us to quantify the average value-at-risk, denoted by $AV@R$, of collision for each region. By integrating RaEM with extensive simulations, the calculated $AV@R$ values achieve a closer resemblance, quantified by the Wasserstein distance, to the ground truth risk compared to existing methods. This signifies that RaEM offers a more accurate assessment of the risk of potential collisions with the environment.

A summary of our contributions includes a novel approach that significantly enhances existing active view acquisition methods for robots. This is achieved by integrating risk assessment directly into the exploration process. Our approach goes beyond merely understanding the environment’s uncertainty such that it also evaluates potential risks associated with different waypoints, allowing robots to operate more safely. Through the combined application of RaEM (Risk-aware Environment Masking) and FisherRF, we equip robots with a more comprehensive awareness of their surroundings. This enables them to navigate safely and make informed decisions in real-world scenarios. All the proofs of the theoretical results are provided in the appendix.

II. MATHEMATICAL NOTATIONS

Throughout the paper, \mathbb{R}^n denotes the n -dimensional Euclidean space and \mathbb{R}_+^n its non-negative orthant. The identity matrix is represented as $I_n \in \mathbb{R}^{n \times n}$. We use $\|x\|_2$ for the Euclidean 2-norm of a vector x . The cardinality of a set \mathcal{X} is denoted by $|\mathcal{X}|$. The set $\mathcal{L}^2(\mathbb{R}^n)$ consists of all \mathbb{R}^n -valued random vectors in a probability space $(\Omega, \mathcal{F}, \mathbb{P})$ with finite second moments. A normal random variable $\mathbf{y} \in \mathbb{R}^n$, with mean $\boldsymbol{\mu} \in \mathbb{R}^n$ and covariance matrix $\Sigma \in \mathbb{R}^{n \times n}$, is denoted as $\mathbf{y} \sim \mathcal{N}(\boldsymbol{\mu}, \Sigma)$. The error function $\text{erf} : \mathbb{R} \rightarrow (-1, 1)$

* G. Liu, W. Jiang, and B. Lei contributed equally to this work.

G. Liu, V. Pandey, and N. Motee are with the Department of Mechanical Engineering and Mechanics, Lehigh University. {gliu, vkp219, motee}@lehigh.edu.

W. Jiang, B. Lei, and K. Daniilidis are with the Department of Computer and Information Science, University of Pennsylvania. {wenjiang, leiboshu}@seas.upenn.edu, {kostas}@cis.upenn.edu

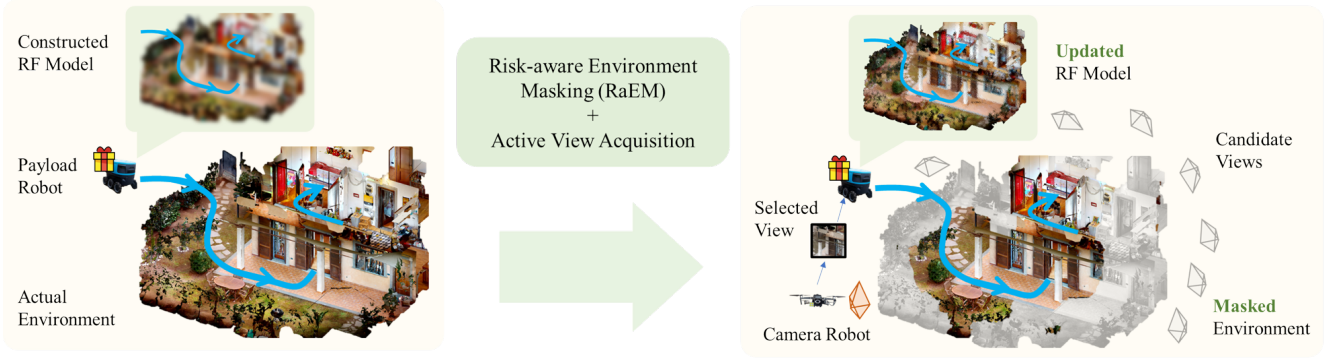


Fig. 1: The payload robot aiming to deliver the asset while the camera robot aims to find the next-best-view to improve the risk assessment.

is defined by $\text{erf}(x) = \frac{2}{\sqrt{\pi}} \int_0^x e^{-t^2} dt$, and is invertible as $\text{erf}^{-1}(x)$ within its range.

III. PROBLEM FORMULATION

We consider a primary payload robot tasked with transporting and delivering an asset to a specific target location, navigating along a pre-specified path $\mathbf{p} = (p_1, p_2, \dots, p_N)$, where each p_i is a waypoint in \mathbb{R}^3 . The onboard processor of the payload robot can generate corresponding actions that navigate itself to the next waypoint. The map of the environment is constructed and stored on the payload robot, which has sufficient computing capabilities to run onboard Radiance Field (RF) models with point-based 3D Gaussian Splatting [9]. The current map is developed by training the RF models with a selected number of sampled views from various viewpoints within the environment.

Given the limited scope of the training data (sampled views), the current RF model will inherently contain a degree of uncertainty, which may make the pre-specified path's safety and risk assessment biased due to the resulting map uncertainty. Thus, there are nonnegligible chances that if the payload robot traverses along the pre-specified path, which satisfies the safety criteria with respect to the current map of the environment, it may still collide with the environment and fail to deliver the asset.

Hence, acquiring a more accurate risk assessment is crucial since it not only allows the payload robot to select a more efficient path with less chance of violating the safety constraints but also prevents the payload robot from underestimating the potential danger and failing in the actual deployment. To enhance safety and avoid biased risk assessment, an auxiliary camera robot, potentially an aerial one, is allowed to travel to certain positions within the environment to collect additional views and share them with the payload robot to update its onboard RF model. This process is depicted in Fig. 1. Given the limited time to complete the task and the onboard computational power, the camera robot has to select the next-best-view from a set of candidate views instead of traversing all candidate viewpoints.

The main *challenge* we address is to enhance the safety and risk assessment of the payload robot's path. Our approach involves selecting the next-best-view from a set of

candidate views supplied by the auxiliary camera robot. By incorporating this chosen view into the existing RF model, we aim to refine and improve only those portions of the environment mapping that are crucial for bolstering the payload robot's safety measures.

IV. TECHNICAL BACKGROUND

In this section, we provide an overview of the RF model and delve into the risk measures for safety evaluation.

A. Volumetric Rendering and Gaussian Splatting

Radiance Field models like 3D Gaussian Splatting [10], Plenoxels [22] leverage volumetric rendering [8] for effectively learning a 3D scene representation from photometric supervision. The pixel color $C(\mathbf{r})$ is determined by integrating colors $c(\mathbf{r}(t))$ weighted by the density $\rho(\mathbf{r}(t))$ along the path of a camera ray $\mathbf{r}(t) = \mathbf{o} + t\mathbf{d}$, which emits from the camera's origin $\mathbf{o} \in \mathbb{R}^3$ and intersects a particular pixel on the image plane, as described by:

$$C(\mathbf{r}) = \int_{t_n}^{t_f} T(t) \rho(\mathbf{r}(t)) c(\mathbf{r}(t), \mathbf{d}) dt, \quad (1)$$

where $T(t) = \exp\left(-\int_{t_n}^t \rho(\mathbf{r}(s)) ds\right)$ represents the cumulative transmittance with t_n and t_f denoting the scene's near and far limits, respectively. NeRF [16] approximates this integral via stratified sampling, expressing it as a weighted sum of sampled points:

$$\hat{C}(\mathbf{r}) = \sum_{i=1}^{N_s} T_i (1 - \exp(-\rho_i \delta_i)) \mathbf{c}_i, \quad (2)$$

$$T_i = \exp\left(-\sum_{j=1}^{i-1} \rho_j \delta_j\right), \quad (3)$$

where $\delta_i = t_{i+1} - t_i$ calculates the interval between consecutive samples, with N_s specifying the sample count. Through this methodology, Radiance Field models refine the 3D scene representation by minimizing the reconstruction errors between the actual captured RGB images $\mathcal{I}_{i=1}^N$ and the computed pixel colors. Although the rendering approach of 3D Gaussian Splatting is distinct from previous NeRF methods, its image formation equation still follows this structure, wherein \mathbf{c}_i denotes the color of each 3D Gaussian, and ρ_i is determined by a 2D Gaussian with covariance Σ

[10, 28]. Following [9], we initialize new 3D Gaussians by unprojecting the RGB-D data on regions outside the rendered silhouette. We also simplified the 3D Gaussian to be isotropic such that its opacity is given by:

$$\rho_i = \epsilon_i \exp\left(-\frac{\|x_i - \mu\|^2}{2r^2}\right), \quad (4)$$

where $x_i \in \mathbb{R}^2$ is the location of the pixel, ϵ is the opacity of the 3D Gaussian and r is the scale of 2D Gaussian projected to the screen. Our scene reconstruction system takes both RGB and depth as input to densely supervise 3D Gaussians. The depth of a pixel is rendered as the weighted sum of depths $d_{dep,i}$ of 3D Gaussians:

$$\mathbf{d}_{dep}(\mathbf{r}) = \sum_{n=1}^{N_s} T_i (1 - \exp(-\rho_n \delta_n)) d_{dep,i}. \quad (5)$$

The scene is optimized with both the RGB rendering loss and the depth supervision:

$$\mathcal{L} = \sum_{r \in R} (\mathcal{L}_1(C(r)) + \gamma \mathcal{L}_1(\mathbf{d}_{dep}(r))) \quad (6)$$

where $\mathcal{L}_1(C(r))$ and $\mathcal{L}_1(\mathbf{d}_{dep}(r))$ are $L1$ loss for RGB and depth respectively, and γ is the weight for the depth loss.

B. Measuring Risk of Collision

To quantify the uncertainty and the safety associated with the relative distances between a specific waypoint (payload robot's position) and mass points in the environment, modeled as 3D Gaussians, we employ the well-known Average Value-at-Risk (AV@R), also known as Conditional Value-at-Risk [21]. AV@R estimates the proximity between the robot and mass points in the most critical scenarios, thus providing insight into the potential severity of near-collision situations. For instance, setting the confidence level at $\varepsilon = 5\%$, AV@R calculates the mean relative distance in the direst 5% of cases, which depicts the scenarios where a collision is most imminent.

Within the probability space $(\Omega, \mathcal{F}, \mathbb{P})$, AV@R [23] of the continuous random variable $y : \Omega \rightarrow \mathbb{R}$, is defined as

$$\text{AV@R}_\varepsilon(y) := \mathbb{E}[y \mid y < \text{V@R}_\varepsilon(y)], \quad (7)$$

where the value-at-risk (V@R) is specified as*:

$$\text{V@R}_\varepsilon(y) := \inf \{z \mid \mathbb{P}\{y < z\} > \varepsilon\}, \quad (8)$$

with $\varepsilon \in (0, 1)$ denoting the confidence level. When the random variable y characterizes the distance, a smaller value of AV@R $_\varepsilon$ indicates a higher chance the collision might happen.

V. COLLISION RISK QUANTIFICATION

The risk of collision between the payload robot and the uncertain environment can be quantified by evaluating the distance between each waypoint and the perceived 3D Gaussians, illustrated as follows.

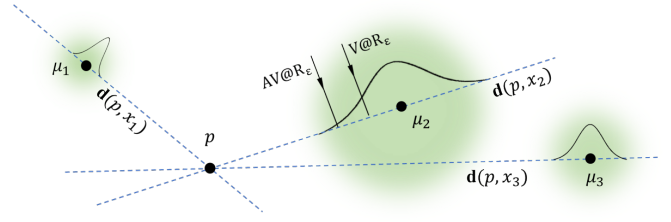


Fig. 2: Distance from waypoint p to 3D Gaussians $x_i \in \mathcal{X}$.

A. Statistics of the Distance to 3D Gaussian Points

We consider the 3D Gaussian representation of the environment as a discrete set \mathcal{X} comprising independent multi-variate normal random variables $x_i \in \mathbb{R}^3$, for $i = 1, \dots, |\mathcal{X}|$, where $|\mathcal{X}|$ is the total number of points within the perceived point cloud. In line with the findings from [9], each point x_i is characterized as $x_i \sim \mathcal{N}(\mu_i, \Sigma_i)^\dagger$, where $\mu_i \in \mathbb{R}^3$ represents the mean (center) position and $\Sigma_i = \sigma_i^2 I_3$ denotes the covariance matrix. Notably, μ_i and σ_i^2 can be accessed from the onboard RF model [7]. We define the random variable that quantifies the distance between a given waypoint and each 3D Gaussian point, as visualized in Fig. 2.

Definition 1. The signed distance between a fixed waypoint $p \in \mathbb{R}^3$ and any 3D Gaussian x_i is defined as

$$d(p, x_i) = \left\langle x_i - p, \frac{\mu_i - p}{\|\mu_i - p\|_2} \right\rangle \in \mathbb{R},$$

where $\langle \cdot, \cdot \rangle$ is the Euclidean inner product.

Furthermore, we show that the signed distance $d(p, x_i)$ is a real-valued normal random variable.

Lemma 1. The signed distance, $d(p, x_i)$, between a fixed waypoint, $p \in \mathbb{R}^3$, and any 3D Gaussian point, $x_i \sim \mathcal{N}(\mu_i, \sigma_i^2 I_3)$, follows a normal distribution, i.e.,

$$d(p, x_i) \sim \mathcal{N}(\|\mu_i - p\|_2, \sigma_i^2).$$

According to Definition 1, the signed distance can take negative values. This means that the realization of the 3D Gaussian x_i might be located on the side opposite to μ_i , relative to p , within the space.

B. Risk of Collision with the Uncertain Environment

Since $d(p, x_i)$ is a continuous random variable, we can quantify the average value-at-risk of a collision with a single 3D Gaussian point as follows.

Theorem 1. Given a waypoint $p \in \mathbb{R}^3$ and a 3D Gaussian point x_i with mean μ_i and covariance matrix $\sigma_i^2 I_3$, the average value-at-risk of a collision can be quantified as:

$$\text{AV@R}_\varepsilon(d(p, x_i)) := \|\mu_i - p\|_2 - \frac{\sigma_i}{\sqrt{2\pi\varepsilon} \exp(\iota_\varepsilon^2)}, \quad (9)$$

*Contrary to the conventional definition [21] $\text{V@R}_\varepsilon := \inf \{z \mid \mathbb{P}\{y > z\} < \varepsilon\}$, it is necessary to consider the opposite tail of the distribution when contemplating collision events.

† In this notation, we focus exclusively on the central position and radius-related parameters of 3D Gaussians, while omitting the color-related parameters as described in [9].

where $\iota_\varepsilon = \text{erf}^{-1}(2\varepsilon - 1)$, and $\varepsilon \in (0, 1)$ represents the desired confidence level.

The value of $\text{AV@R}_\varepsilon(d(p, x_i))$ represents the expected conditional outcome when the distance between the waypoint and the 3D Gaussian point falls below a certain threshold, i.e., $V@R_\varepsilon$, as illustrated in Fig. 2. A lower $\text{AV@R}_\varepsilon(d(p, x_i))$ signifies a higher risk of the payload robot colliding with the 3D Gaussian point.

While AV@R_ε effectively captures the collision risk for the payload robot, a more intuitive representation of this risk can be created by assigning a real number within $[0, \infty]$ to quantify the “dangerousness” of the scenario. This approach uses a family of level sets, defined by

$$C_\delta = \left(-\infty, \frac{d_s}{1 + \delta} \right), \quad (10)$$

where $d_s > 0$ is a predefined cutoff distance. Here, the payload robot is deemed safe if $\{d(p, x_i) \notin C_0\}$, and a collision event is defined as $\{d(p, x_i) \in C_\infty\}$. Accordingly, the associated collision risk, as defined in [14], is

$$\mathcal{A}_\varepsilon(d(p, x_i)) = \sup \left\{ \delta \geq 0 \mid \text{AV@R}_\varepsilon(d(p, x_i)) \in C_\delta \right\}.$$

Theorem 2. For any given waypoint $p \in \mathbb{R}^3$ and a 3D Gaussian $x_i \sim \mathcal{N}(\mu_i, \sigma_i^2 I_3)$, the risk of collision with respect to the level sets is

$$\mathcal{A}_\varepsilon(d(p, x_i)) := \begin{cases} 0, & \text{if } \frac{\mu - d_s}{\sigma_i} \geq \kappa_\varepsilon \\ \frac{d_s}{\mu - \kappa_\varepsilon \sigma_i} - 1, & \text{if } \kappa_\varepsilon \in \left(\frac{\mu - d_s}{\sigma_i}, \frac{\mu}{\sigma_i} \right) \\ \infty, & \text{if } \frac{\mu}{\sigma_i} \leq \kappa_\varepsilon \end{cases},$$

where $\mu = \|\mu_i - p\|_2$, $\kappa_\varepsilon = (\sqrt{2\pi\varepsilon} \exp(\iota_\varepsilon^2))^{-1}$, and $\iota_\varepsilon = \text{erf}^{-1}(2\varepsilon - 1)$.

This new risk representation, as described above, quantifies the danger similarly to Theorem 1 but offers a more intuitive understanding. A higher value of \mathcal{A}_ε directly translates to a greater chance of a collision and potentially more severe consequences.

For any specified waypoint p_k in \mathbf{p} , there are $|\mathcal{X}|$ corresponding risk values, each linked to a distinct 3D Gaussian point x_i . In this paper, we focus on the most dangerous scenario, characterized by the lowest AV@R_ε , to represent the risk of collision with the uncertain environment at p_k . This is expressed as:

$$\alpha_k = \min_{x_i \in \mathcal{X}} \text{AV@R}_\varepsilon(d(p_k, x_i)), \quad (11)$$

highlighting the worst-case collision risk in the current perceived environment.

VI. RISK-AWARE ENVIRONMENT MASKING AND THE NEXT BEST VIEW IN THE MASKED ENVIRONMENT

To improve risk assessment during the payload robot’s navigation, our strategy focuses on a limited set of 3D Gaussian points near each waypoint. This involves masking out irrelevant parts of the environment and then choosing the next-best-view based on this masked environment.

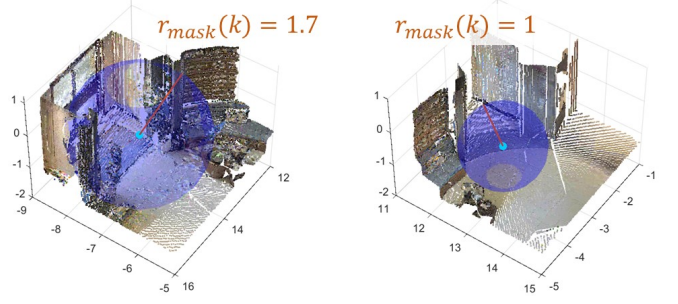


Fig. 3: Masking radius of RaEM.

A. Risk-Aware Environment Masking

Risk-aware environment masking (RaEM) centers around a sphere. This sphere, with a radius of $r_{mask}(k) > 0$, is drawn around each waypoint p_k on the path. The radius is determined by the potential risk the uncertain environment poses to the robot at each waypoint.

Definition 2. (Masking Radius) The masking radius at each waypoint p_k is defined as:

$$r_{mask}(k) = \beta_1 \cdot e^{-\beta_2 \cdot \alpha_k}, \quad (12)$$

where β_1 and β_2 are predetermined positive constants that control the sensitivity of the masking radius to the risk level.

A key aspect of RaEM is the dynamic masking radius, which adapts based on the robot’s perceived risk at each waypoint. In high-risk situations (indicated by a lower α_k value), the radius increases, prompting the robot to cautiously focus on a larger area around the waypoint for a more thorough assessment. Conversely, in lower-risk scenarios (higher α_k value), the radius decreases, allowing the robot to explore a wider surrounding area without excessive attention on less critical regions. This approach ensures the robot prioritizes scrutinizing safety-critical zones within the environment, as illustrated in Fig. 3. Mathematically, the masked environment after applying RaEM is a subset of the original environment, containing only the points that fall within the union of spheres centered at each waypoint. For a given path $\mathbf{p} = (p_1, \dots, p_N)$, these spheres have radii determined by the masking function, defined as:

$$\mathcal{M}(\mathbf{p}) = \left\{ x \in \mathcal{X} \mid x \in \bigcup_{k=1}^N \mathcal{B}(p_k, r_{mask}(k)) \right\} \quad (13)$$

Here, $\mathcal{B}(p_k, r_{mask}(k))$ represents a 3D ball centered at p_k with radius $r_{mask}(k)$. This dynamic masking process refines the robot’s focus based on the perceived risk level, enabling a more efficient and risk-aware navigation strategy.

B. Next Best View with Respect to RaEM

Having characterized the masked environment, our next step involves quantifying the informativeness of each candidate view. The aim is to select the most informative view that will improve the accuracy of risk assessment for the close proximity to the path \mathbf{p} . To accomplish this, we provide a brief introduction to the view selection algorithm [7],

which utilizes the Expected Information Gain (EIG) at each candidate view.

The Fisher Information serves as a measure of the information that an observation pair (\mathbf{x}, Φ) carries about the unknown parameters \mathbf{w} that define the model $p(\Phi|\mathbf{x}; \mathbf{w})$. In the context of novel view synthesis, the pair (\mathbf{x}, Φ) correspond to the camera pose \mathbf{x} and the image observation Φ at that pose, respectively. Here, \mathbf{w} represents the parameters of the radiance field. The primary objective in neural rendering is to minimize the negative log-likelihood (NLL) between the rendered images and ground truth images in the holdout set. This minimization is inherently indicative of the scene reconstruction quality, as defined by

$$-\log \mathbb{P}(\Phi|\mathbf{x}, \mathbf{w}) = (\Phi - f(\mathbf{x}, \mathbf{w}))^T (\Phi - f(\mathbf{x}, \mathbf{w})), \quad (14)$$

where $f(\mathbf{x}, \mathbf{w})$ represents the onboard rendering model with 3D Gaussians. Under the regularity conditions [25], the Fisher Information corresponding to the model $\log \mathbb{P}(\Phi|\mathbf{x}; \mathbf{w})$ is characterized as the Hessian of the log-likelihood function with respect to the model parameters \mathbf{w} :

$$\mathcal{I}(\mathbf{w}) = -\mathbb{E}_{p(\Phi|\mathbf{x}, \mathbf{w})} \left[\frac{\partial^2 \log p(\Phi|\mathbf{x}, \mathbf{w})}{\partial \mathbf{w}^2} \right] \Big|_{\mathbf{w}} = \mathbf{H}''[\Phi|\mathbf{x}, \mathbf{w}],$$

where $\mathbf{H}''[\Phi|\mathbf{x}, \mathbf{w}]$ is the Hessian matrix of (14).

In the context of the active view selection problem, we initiate the process with a training set D^{train} and obtain an initial estimation of parameters \mathbf{w}^* using D^{train} . Our main objective is to identify the next-best-view that maximizes the Expected Information Gain [13, 6, 11] among potential viewpoints $\mathbf{x}_i^{acq} \in D^{pool}$ in comparison to D^{train} , where D^{pool} denotes the collection of available views:

$$\begin{aligned} \mathcal{I}[\mathbf{w}^*; \{\Phi_i^{acq}\}|\{\mathbf{x}_i^{acq}\}, D^{train}] \\ = H[\mathbf{w}^*|D^{train}] - H[\mathbf{w}^*|\{\Phi_i^{acq}\}, \{\mathbf{x}_i^{acq}\}, D^{train}] \end{aligned} \quad (15)$$

where $H[\cdot]$ is the entropy [12]. The relation between D^{train} and D^{pool} is also depicted in Fig. 4.

Given the log-likelihood's expression as in (14), specifically the rendering error in our context, the entropy difference on the right-hand side of (15) can be estimated as follows [12]:

$$\begin{aligned} \frac{1}{2} \log \det (\mathbf{H}''[\{\Phi_i^{acq}\}|\{\mathbf{x}_i^{acq}\}, \mathbf{w}^*] \mathbf{H}''[\mathbf{w}^*|D^{train}]^{-1} + I) \\ \leq \frac{1}{2} \text{tr} (\mathbf{H}''[\{\Phi_i^{acq}\}|\{\mathbf{x}_i^{acq}\}, \mathbf{w}^*] \mathbf{H}''[\mathbf{w}^*|D^{train}]^{-1}). \end{aligned}$$

Since Fisher Information is additive, $\mathbf{H}''[\mathbf{w}^*|D^{train}]^{-1}$ can be computed by aggregating the Hessian of model parameters from all viewpoints in $\{D^{train}\}$ prior to inversion. The forthcoming optimal view \mathbf{x}_i^{acq} is selected by:

$$\arg \max_{\mathbf{x}_i^{acq}} \text{tr} (\mathbf{H}''[\Phi_i^{acq}|\mathbf{x}_i^{acq}, \mathbf{w}^*] \mathbf{H}''[\mathbf{w}^*|D^{train}]^{-1}). \quad (16)$$

The model's Hessian $\mathbf{H}''[\Phi|\mathbf{x}, \mathbf{w}^*]$ is determined as:

$$\begin{aligned} \mathbf{H}''[\Phi|\mathbf{x}, \mathbf{w}^*] = \\ \nabla_{\mathbf{w}} f(\mathbf{x}; \mathbf{w}^*)^T \nabla_{f(\mathbf{x}; \mathbf{w}^*)}^2 H[\Phi|f(\mathbf{x}; \mathbf{w}^*)] \nabla_{\mathbf{w}} f(\mathbf{x}; \mathbf{w}^*) \end{aligned} \quad (17)$$

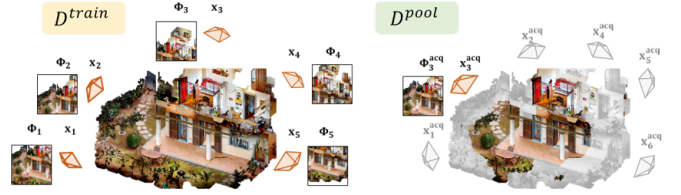


Fig. 4: Observation pairs $(\mathbf{x} \in D^{train}, \Phi)$ and candidate observation pairs $(\mathbf{x}^{acq} \in D^{pool}, \Phi^{acq})$.

where $\mathbf{H}''[\Phi|\mathbf{x}, \mathbf{w}^*]$ in our case is equal to the covariance of the RGB measurement that we set equal to one. Thus, the Hessian matrix can be computed solely using the Jacobian matrix of $f(\mathbf{x}, \mathbf{w})$:

$$\mathbf{H}''[\Phi|\mathbf{x}, \mathbf{w}^*] = \nabla_{\mathbf{w}} f(\mathbf{x}; \mathbf{w}^*)^T \nabla_{\mathbf{w}} f(\mathbf{x}; \mathbf{w}^*). \quad (18)$$

This optimization of the objective in (16) is feasible without the ground truth of the candidate views' ground truths $\{\Phi_i^{acq}\}$, as expected since Fisher Information is independent of the observations. The Hessian in (18) possesses a limited number of non-diagonal elements since each pixel's independence is considered in $-\log p(\Phi|\mathbf{x}, \mathbf{w})$. Moreover, recent NeRF models [3, 17, 20, 26] typically use structured local parameters whereby each parameter influences only the radiance and density within a confined spatial domain, aiding in expedited convergence and rendering. Thus, only parameters affecting the pixel colors have non-zero entries in the Hessian matrix $\mathbf{H}''[\Phi|\mathbf{x}, \mathbf{w}^*]$. Nevertheless, with the parameter count often exceeding 200 million, computing without sparsification or approximation is unfeasible. Practically, the Laplace approximation method [2, 15] is employed, approximating the Hessian matrix with its diagonal components and a log-prior regularizer λI :

$$\mathbf{H}''[\Phi|\mathbf{x}, \mathbf{w}^*] \approx \text{diag}(\nabla_{\mathbf{w}} f(\mathbf{x}, \mathbf{w}^*)^T \nabla_{\mathbf{w}} f(\mathbf{x}, \mathbf{w}^*)) + \lambda I. \quad (19)$$

This approximation further simplifies the inversion of the Hessian matrix $\mathbf{H}''[\Phi|\mathbf{x}, \mathbf{w}^*]$.

VII. EXPERIMENTS

As illustrated in Fig. 1, our experiments consist of a payload robot deployed to the ground inside a simulated environment and an aerial camera robot that is capable of maneuvering, collecting novel views, and sharing them with the payload robot.

A. Experiment Setup

The simulated environment is constructed with the Habitat simulator [24], and we use scenes from the Matterport3D [1] dataset for our experiments. We follow the extensions of SplatAM [9] on 3D Gaussian Splatting [10] to build the scene representation for the environment. In each scene, the payload robot will follow a predefined path \mathbf{p} that consists of 10 waypoints to deliver the asset. Considering the fact that the time to complete the task and the computational power is limited, the camera robot is only allowed to capture the novel view when it arrives at the candidate viewpoint. The

$\mathbb{W}_2(\mathbb{P}, \hat{\mathbb{P}}) \downarrow$	Method		
Scene ID		FisherRF	FisherRF + RaEM
YVUC4YcDtcY		0.8021	0.5770
2t7WUuJeko7		0.4667	0.4063
ARNzJeq3xxb		0.5591	0.5113
RPmz2sHmrrY		0.5266	0.2335
Vt2qJdWjCF2		0.6960	0.6565
q9vSo1VnCiC		0.9547	0.6706
WYY7iVyf5p8		0.4547	0.4399
pa4otMbVnkk		0.7471	0.5644
fzynW3qQPVF		1.0088	0.8004
yqstnuAEVhm		0.6889	0.3698

TABLE I: The comparison between $\mathbb{W}_2(\mathbb{P}, \hat{\mathbb{P}})$ and $\mathbb{W}_2(\mathbb{P}^{\text{RaEM}}, \hat{\mathbb{P}})$ within various scenes from Matterport3D.

camera robot is allowed to take a total of 11 views to train and update the RF model, in which the candidate views are generated in three stages:

- Stage 1: A fixed initial view is fed to the payload robot.
- Stage 2: Select 5 views, a total of 250 candidate views are randomly generated within a proximity of radius 2 along the path \mathbf{p} .
- Stage 3: Select 5 views, a total of 250 candidate views are randomly generated within a proximity of radius 2 w.r.t. the center of the explored environment.

The payload robot will use the first 1+5 views to construct the initial representation of the environment at Stage 1 and 2. Then, it will use the next 5 views to enhance the current RF model via Stage 3. At all stages, the next-best-view is selected by maximizing the expected information gain (16) as in FisherRF [7]. At Stage 3, when RaEM is activated, the next-best-view is selected by solving (16) in the masked environment.

B. Implementation Details

At Stage 1, the camera robot captures an RGB-D observation of the environment with the size of 256×256 , and the onboard RF model with 3D Gaussian Splatting is trained with the initial view for 60 iterations. At Stages 2 and 3, the view selection algorithm [7] is implemented among the randomly generated candidate views, in which we implement the computation of the Fisher Information on 3D Gaussian Splatting [10] with customized CUDA kernels as in [7]. The log-prior regularizer λ in (14) is 0.1 and the depth loss weight γ is 0.5 across all experiments. Once the next view is selected, the camera robot uses the pathfinder provided by Habitat API to find the shortest action lists to the target viewpoint. Then, the onboard RF model will be optimized for 60 iterations with each collected RGB-D observation at both Stages 2 and 3, indicating a total of 660 iterations for each experiment. During RaEM, AV@R is evaluated with confidence level $\varepsilon = 0.1$ and the masking parameters are set as $\beta = 0.2$ and $\beta_2 = 1$ for all experiments.

C. Effectiveness of RaEM

By shifting the focus of the next-best-view to the masked environment with RaEM, the RF model will utilize the

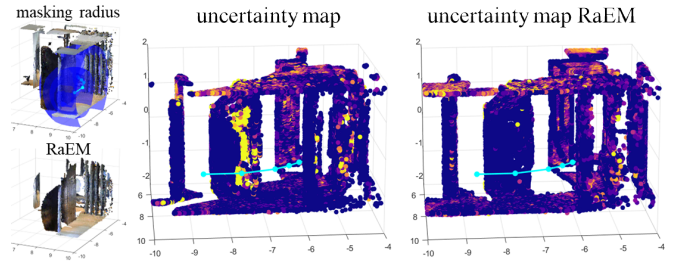


Fig. 5: Uncertainty map comparison in the safety-critical region.

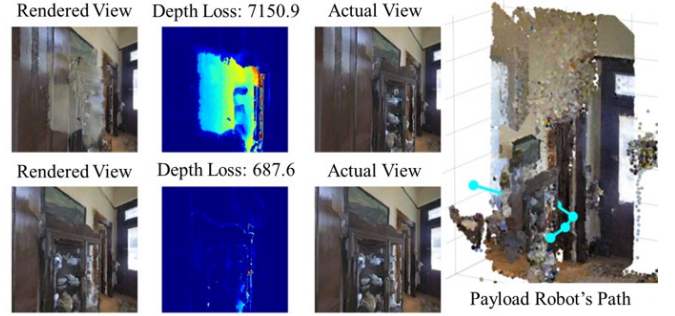


Fig. 6: View and depth comparison in the safety-critical region. Top: Views w/o RaEM. Bottom: Views w/ RaEM.

limited novel views on the safety-critical subset of the environment, as depicted in Fig. 7. To illustrate the effectiveness of RaEM, we evaluate the distribution of the closest distance[‡] from the payload robot to the environment. The resulting distributions are denoted as \mathbb{P}^{RaEM} and \mathbb{P} for using RaEM and not using RaEM, respectively. Then, we quantify the distribution of the closest distance to the environment using the ground truth point clouds as $\hat{\mathbb{P}}$, which are the ground truth 3D Gaussians obtained from the environment, represented by $\hat{x}_i \in \hat{\mathcal{X}}$. It is assumed that \hat{x}_i follows a normal distribution $\hat{x}_i \sim \mathcal{N}(\hat{\mu}_i, \hat{\sigma}_i^2)$, in which $\hat{\mu}_i \in \mathbb{R}^3$ denotes the ground truth position, and $\hat{\sigma}_i$ is a positive real value that is close to 0.

The Wasserstein distance measures the distances between two probability distributions, and the type-2 Wasserstein distance [5] between two normal distributions \mathbb{P} with (μ, σ) and $\hat{\mathbb{P}}$ with $(\hat{\mu}, \hat{\sigma})$ is given by

$$\mathbb{W}_2(\mathbb{P}, \hat{\mathbb{P}}) = \sqrt{\|\mu - \hat{\mu}\|_2^2 + (\sigma - \hat{\sigma})^2},$$

where \mathbb{P} is the distribution of the closet distance to the perceived 3D Gaussians (with or without RaEM), and $\hat{\mathbb{P}}$ is the ground truth distribution of the closet distance. The above quantity measures how much the constructed 3D scene representation deviates from the ground truth scene in the safety-critical regions. In Table I, the effectiveness of RaEM is shown by comparing $\mathbb{W}_2(\mathbb{P}_i^{\text{RaEM}}, \hat{\mathbb{P}}_i)$ and $\mathbb{W}_2(\mathbb{P}_i, \hat{\mathbb{P}}_i)$.

The effectiveness of RaEM is further illustrated in Fig. 5, in which RaEM selects views that focus on the safety-critical region of the environment, resulting in a less uncertain scene

[‡]The closest point is determined in terms of AV@R_ε , which can be quantified as $d(p_k, \arg \min_{x_i} \text{AV@R}_\varepsilon(d(p, x_i)))$.

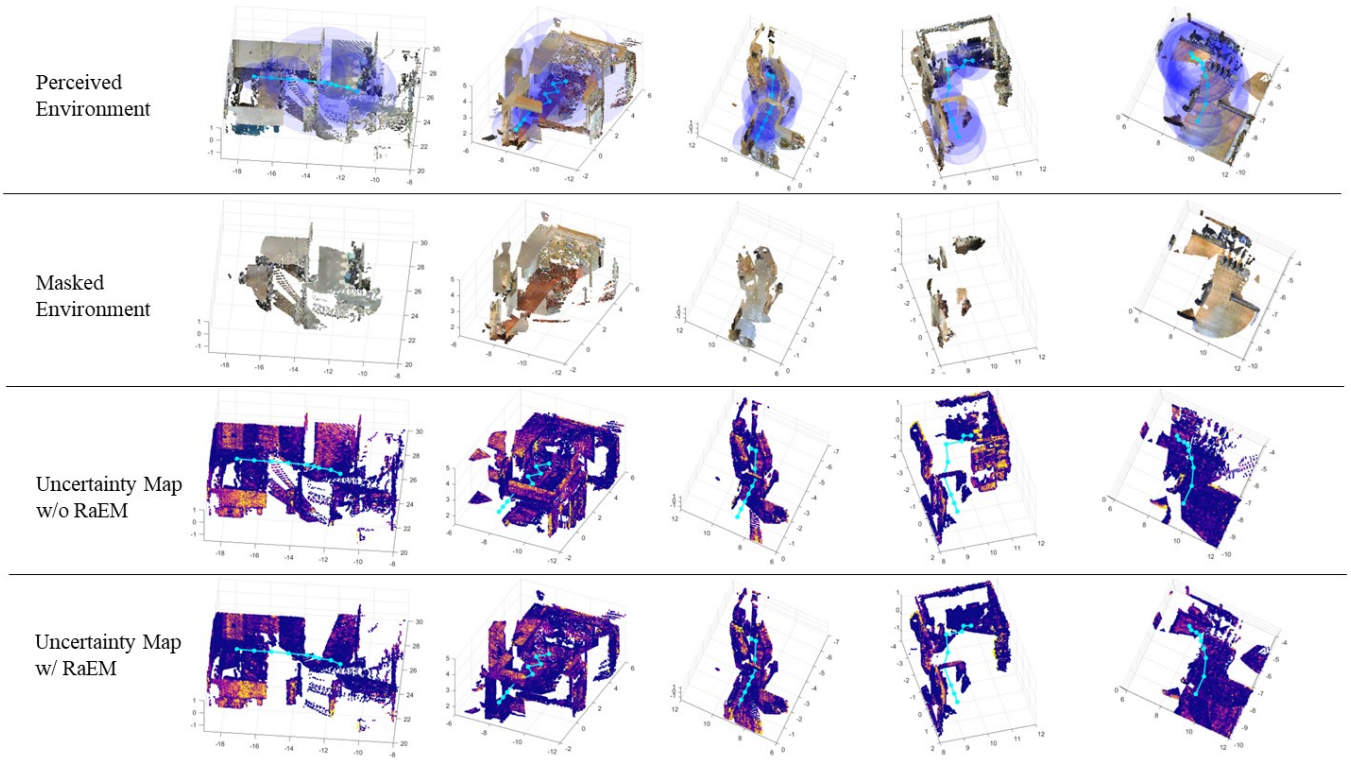


Fig. 7: Perceived map and uncertainty map among various scenes of Matterport3D (scene ID: ‘YVUC4YcDtcY’ ‘yqstnuAEVhm’ ‘pa4otMbVnkk’ ‘RPMz2sHmrrY’ ‘fzynW3qQPVF’). The pre-defined path is shown in aqua color, and a darker uncertainty map [7] indicates less uncertainty.

Method	Uniform Radius					RaEM
$r_{mask}(k)$	3	2	1	0.5	0.1	$\beta_1 e^{-\beta_2 \alpha_k}$
$\mathbb{W}_2(\mathbb{P}, \mathbb{P}) \downarrow$	0.488	0.494	0.559	0.392	N/A	0.370

TABLE II: Comparison between RaEM and uniform radius.

construction. A similar phenomenon is also observed in Fig. 6, in the safety-critical region, the RF model with RaEM obtains a better image rendering quality and more accurate depth estimation.

D. Dynamic Masking via Risk-awareness

In addition to the advancement of highlighting the safety-critical proximity of the payload robot, RaEM also offers dynamic adjustments of the masking radius based on the dangerousness of the current waypoint. An intuitive way of highlighting the safety-critical region can be achieved by setting a constant uniformed masking radius along the path \mathbf{p} . In this case, the environment masking is accomplished by setting $r_{mask}(k) = 1.5$ in (13), for instance. In Fig. 8 (a), it is shown that RaEM can effectively concentrate more on the safety-critical regions while uniform radius will treat all the 3D Gaussians equally in its proximity, which is also validated in Table II with various masking radii.

In addition to $AV@R_\epsilon(d(p_k, x_i))$, other common risk measures such as the expected value $\mathbb{E}[d(p_k, x_i)]$ can also be used to dynamically mask the environment by using (12). However, in situations when the pre-specified path is close

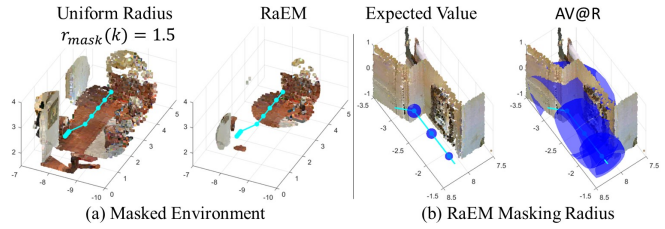


Fig. 8: Comparison of masked environment and masking radius.

to the uncertain environment, unlike $AV@R_\epsilon(d(p_k, x_i))$, $\mathbb{E}[d(p_k, x_i)]$ will underestimate the collision risk and fail to take the safety-critical region into account, see Fig. 8 (b).

VIII. CONCLUSION

In this paper, we proposed an active view acquisition framework that focuses on enhancing the risk and safety assessment while concurrently advancing 3D scene construction. By harnessing Radiance Field models and 3D Gaussian Splatting, our approach, integrated with Risk-aware Environment Masking (RaEM), facilitates the selection of the next-best-view to maximize information gain. Through this strategy, we aim to mitigate potential hazards and uncertainties along pre-specified robot trajectories, thus enhancing both safety and efficiency in the robot’s navigation. The experimental results showcased the efficacy of our method in near real-world scenarios, underscoring its potential to

revolutionize the broader landscape of robotic systems and autonomous navigation. This work represents a significant stride towards establishing a more resilient and safety-centric framework for active robot exploration and comprehensive 3D scene understanding.

APPENDIX

Proof of Lemma 1: The result is immediate by evaluating the marginal distribution of $(x_i - p) \sim \mathcal{N}(\mu_i - p, \sigma_i I_3)$ along the vector $\frac{\mu_i - p}{\|\mu_i - p\|_2}$ such that the marginal mean is

$$\left(\frac{\mu_i - p}{\|\mu_i - p\|_2}\right)^T (x_i - p) = \|\mu_i - p\|_2,$$

and the variance

$$\left(\frac{\mu_i - p}{\|\mu_i - p\|_2}\right)^T \sigma_i^2 I_3 \frac{\mu_i - p}{\|\mu_i - p\|_2} = \sigma_i^2. \quad \square$$

Proof of Theorem 1: Given the fact that the position of the 3D Gaussian point x_i follows a normal distribution, one has

$$\mathbb{P}\{d(p, x_i) < z\} = \frac{1}{2} \left(1 + \operatorname{erf}\left(\frac{z - \mu}{\sqrt{2}\sigma_i}\right)\right),$$

and considering the fact that the probability density function of the normal distribution is continuous,

$$V@R_\varepsilon(d(p, x_i)) = \sqrt{2}\sigma_i \operatorname{erf}^{-1}(2\varepsilon - 1) + \|\mu_i - p\|_2.$$

The corresponding AV@R is evaluated by using change of variable such that

$$\begin{aligned} AV@R_\varepsilon(d(p, x_i)) &= \frac{1}{\varepsilon} \int_{-\infty}^{V@R_\varepsilon(d(p, x_i))} z \frac{1}{\sqrt{2\pi}\sigma_i} \exp\left(-\frac{(z - \mu)^2}{2\sigma_i^2}\right) dz \\ &= \mu - \frac{\sigma_i}{\sqrt{2\pi}\varepsilon \exp(\iota_\varepsilon^2)}, \end{aligned}$$

where $\mu = \|\mu_i - p\|_2$ and $\iota_\varepsilon = \operatorname{erf}^{-1}(2\varepsilon - 1)$. \square

Proof of Corollary 2: Given that the probability density function of $d(p, x_i)$ is continuous, one can represent the risk in terms of level sets by considering when $AV@R_\varepsilon(d(p, x_i)) > \frac{r}{\delta+c}$, $AV@R_\varepsilon(d(p, x_i)) < 0$, and $AV@R_\varepsilon(d(p, x_i)) \in (0, \frac{r}{\delta+c})$. Then, middle branch is obtained by solving for $AV@R_\varepsilon(d(p, x_i)) = \frac{r}{\delta+c}$. \square

REFERENCES

- [1] A. Chang et al. “Matterport3D: Learning from RGB-D Data in Indoor Environments”. In: *International Conference on 3D Vision* (2017).
- [2] E. Daxberger, A. Kristiadi, A. Immer, R. Eschenhagen, M. Bauer, and P. Hennig. “Laplace Redux—Effortless Bayesian Deep Learning”. In: *NeurIPS*. 2021.
- [3] S. Fridovich-Keil, A. Yu, M. Tancik, Q. Chen, B. Recht, and A. Kanazawa. “Plenoxels: Radiance fields without neural networks”. In: *Proceedings of the IEEE/CVF Conference on Computer Vision and Pattern Recognition*. 2022, pp. 5501–5510.
- [4] G. Georgakis, B. Bucher, A. Arapin, K. Schmeckpeper, N. Matni, and K. Daniilidis. “Uncertainty-driven planner for exploration and navigation”. In: *2022 International Conference on Robotics and Automation (ICRA)*. IEEE. 2022, pp. 11295–11302.
- [5] C. R. Givens and R. M. Shortt. “A class of Wasserstein metrics for probability distributions.” In: *Michigan Mathematical Journal* 31.2 (1984), pp. 231–240.
- [6] N. Houlsby, F. Huszar, Z. Ghahramani, and M. Lengyel. “Bayesian Active Learning for Classification and Preference Learning”. In: *CoRR* abs/1112.5745 (2011).
- [7] W. Jiang, B. Lei, and K. Daniilidis. “FisherRF: Active View Selection and Uncertainty Quantification for Radiance Fields using Fisher Information”. In: *arXiv preprint arXiv:2311.17874* (2023).
- [8] J. T. Kajiya and B. P. Von Herzen. “Ray tracing volume densities”. In: *ACM SIGGRAPH computer graphics* 18.3 (1984), pp. 165–174.
- [9] N. Keetha et al. “Splatam: Splat, track & map 3d gaussians for dense rgb-d slam”. In: *arXiv preprint arXiv:2312.02126* (2023).
- [10] B. Kerbl, G. Kopanas, T. Leimkühler, and G. Drettakis. “3D Gaussian Splatting for Real-Time Radiance Field Rendering”. In: *ACM Transactions on Graphics* 42.4 (July 2023).
- [11] A. Kirsch, J. v. Amersfoort, and Y. Gal. “BatchBALD: Efficient and Diverse Batch Acquisition for Deep Bayesian Active Learning”. In: *NeurIPS*. 2019.
- [12] A. Kirsch and Y. Gal. “Unifying Approaches in Active Learning and Active Sampling via Fisher Information and Information-Theoretic Quantities”. In: *Transactions on Machine Learning Research* (2022). Expert Certification. ISSN: 2835-8856.
- [13] D. V. Lindley. “On a Measure of the Information Provided by an Experiment”. In: *The Annals of Mathematical Statistics* 27.4 (1956).
- [14] G. Liu, C. Somarakis, and N. Motee. “Risk of Cascading Collisions in Network of Vehicles with Delayed Communication”. In: *arXiv preprint arXiv:2312.17147* (2023).
- [15] D. J. C. MacKay. “Bayesian Interpolation”. In: *Neural Computation* 4.3 (May 1992), pp. 415–447.
- [16] B. Mildenhall, P. P. Srinivasan, M. Tancik, J. T. Barron, R. Ramamoorthi, and R. Ng. “NeRF: Representing Scenes as Neural Radiance Fields for View Synthesis”. In: *ECCV*. 2020.
- [17] T. Müller, A. Evans, C. Schied, and A. Keller. “Instant neural graphics primitives with a multiresolution hash encoding”. In: *ACM Transactions on Graphics (ToG)* 41.4 (2022), pp. 1–15.
- [18] X. Pan, Z. Lai, S. Song, and G. Huang. “Activenerf: Learning where to see with uncertainty estimation”. In: *European Conference on Computer Vision*. Springer. 2022, pp. 230–246.
- [19] Y. Ran et al. “NeurAR: Neural Uncertainty for Autonomous 3D Reconstruction With Implicit Neural Representations”. In: *IEEE Robotics and Automation Letters* 8.2 (2023), pp. 1125–1132.
- [20] C. Reiser, S. Peng, Y. Liao, and A. Geiger. “Kilonerf: Speeding up neural radiance fields with thousands of tiny mlps”. In: *Proceedings of the IEEE/CVF International Conference on Computer Vision*. 2021, pp. 14335–14345.
- [21] R. T. Rockafellar and S. Uryasev. “Conditional value-at-risk for general loss distributions”. In: *Journal of Banking and Finance* 26.7 (2002), pp. 1443–1471.
- [22] Sara Fridovich-Keil and Alex Yu, M. Tancik, Q. Chen, B. Recht, and A. Kanazawa. “Plenoxels: Radiance Fields without Neural Networks”. In: *CVPR*. 2022.
- [23] S. Sarykalin, G. Serrano, and S. Uryasev. “Value-at-risk vs. conditional value-at-risk in risk management and optimization”. In: *State-of-the-art decision-making tools in the information-intensive age*. Informa, 2008, pp. 270–294.
- [24] M. Savva et al. “Habitat: A Platform for Embodied AI Research”. In: *Proceedings of the IEEE/CVF International Conference on Computer Vision (ICCV)*. 2019.
- [25] M. J. Schervish. *Theory of statistics*. Springer Science & Business Media, 2012.
- [26] C. Sun, M. Sun, and H.-T. Chen. “Direct voxel grid optimization: Super-fast convergence for radiance fields reconstruction”. In: *Proceedings of the IEEE/CVF Conference on Computer Vision and Pattern Recognition*. 2022, pp. 5459–5469.
- [27] Z. Yan, H. Yang, and H. Zha. “Active neural mapping”. In: *Proceedings of the IEEE/CVF International Conference on Computer Vision*. 2023, pp. 10981–10992.
- [28] W. Yifan, F. Serena, S. Wu, C. Öztireli, and O. Sorkine-Hornung. “Differentiable surface splatting for point-based geometry processing”. In: *ACM Transactions on Graphics (TOG)* 38.6 (2019).
- [29] H. Zhan, J. Zheng, Y. Xu, I. Reid, and H. Rezaeifighi. “ActiveRMAP: Radiance Field for Active Mapping And Planning”. In: *arXiv preprint arXiv:2211.12656* (2022).